

# Proline-Derived Structural Phases on Cu{311}

David C. Madden<sup>1</sup> · Israel Temprano<sup>1</sup> · Stephen J. Jenkins<sup>1</sup> · Stephen M. Driver<sup>1</sup>

Published online: 30 May 2015

© The Author(s) 2015. This article is published with open access at Springerlink.com

**Abstract** Structural phases formed by adsorption of L-proline onto a Cu{311} surface in ultra-high vacuum were investigated using reflection–absorption infrared spectroscopy, low-energy electron diffraction and scanning tunnelling microscopy. An ordered structural phase formed by self-assembly of L-prolinate with (2,1;1,2) periodicity, and a transition from pure  $\mu_3$  bonding to a mixture of  $\mu_3$  and  $\mu_2$  bonding with increasing exposure at 300 K, were observed. This behaviour has broad parallels with that previously seen with alaninate and glycinate on Cu{311}, but the detailed correlation between structure and bonding, and their evolution during subsequent annealing, are markedly different for prolinate as compared to alaninate and glycinate. At annealing temperatures around 480–490 K, a new structural phase with (5,3;4,6) periodicity emerges. We tentatively attribute this to pyrrole-2-carboxylate, formed by dehydrogenation and aromatization of the pyrrolidine ring of prolinate. The observation of equal areas of the two possible mirror domains associated with the two possible adsorbate–substrate bonding enantiomers implies a prochiral intermediate.

**Keywords** Chiral · Enantioselectivity · Heterogeneous catalysis · Self-organization · Alanine · Glycine

---

Additional data related to this publication are available at the DSpace@Cambridge repository (<https://www.repository.cam.ac.uk/handle/1810/248026>).

---

✉ Stephen J. Jenkins  
sjj24@cam.ac.uk

✉ Stephen M. Driver  
smd37@cam.ac.uk

<sup>1</sup> Department of Chemistry, University of Cambridge, Lensfield Road, Cambridge CB2 1EW, UK

## 1 Introduction

The overlayers that form when simple  $\alpha$ -amino acids adsorb at single-crystal Cu surfaces have proved to be fertile ground for investigating how chirality can be manifested at solid surfaces [1–23]. Molecular adsorption of an enantiopure  $\alpha$ -amino acid (excepting glycine, which lacks a chiral centre) necessarily imposes chirality on even a high-symmetry crystalline surface. Chirality may also arise specifically from the configuration of the bonding between adsorbate and substrate: this is known as “footprint chirality”. For example, the  $\mu_3$  bonding configuration preferred by both glycine and alanine adsorbed, in anionic form, on Cu{110} places the amine N and both carboxylate O atoms near-atop Cu atoms. Due to the rectangular shape of the {110}-(1 × 1) unit mesh, the three Cu atoms to which the adsorbate bonds are arranged in the form of a right-angled scalene triangle, which can exist in either of two mirror-equivalent enantiomeric forms (the mirror symmetry of the pure geometric form being broken by the presence of the underlying surface). In consequence, the adsorbate–substrate bonding configuration is chiral; this is true even for the glycinate–surface complex, despite the mirror symmetry of the Cu{110} surface and the absence of a molecular chiral centre. At higher coverages of enantiopure alaninate on Cu{110}, with the onset of 2-point “ $\mu_2$ ” bonding (involving the amine group and a single carboxylate O), chirality emerges in the long-range self-assembly, with the 2D surface lattice (i.e. the disposition of lattice points, irrespective of atomic positions in the surface motif) becoming chiral.

A complementary line of enquiry is to reduce the mirror symmetry of the metal surface by means of the choice of surface orientation. Indeed, one can choose a high-index surface orientation that is devoid of any mirror symmetry

and thus is intrinsically chiral. This has motivated studies of Cu{531}, for example [24–28]. From the point of view of amino acid adsorption, however, Cu{311} provides a particularly interesting counterpoint to Cu{110}. Although the crystallographic differences are relatively subtle, the {311} surface, shown schematically in Fig. 1a, has less mirror symmetry than {110} (one mirror plane instead of two), and no rotational symmetry. It does, however, offer potential adsorption sites for  $\mu_3$ -bonded amino acids in which the three Cu atoms to which the adsorbate bonds are arranged in the form of an isosceles (i.e. mirror-symmetric) triangle. One might therefore predict that the footprint chirality seen for  $\mu_3$  bonding on Cu{110} will be “switched off” on {311}. Experiments with glycine and alanine have confirmed this prediction [27, 29–31]: both species give rise a ‘symmetric lattice’ (SL) overlayer in which each (2,1;1,2) unit mesh contains a single  $\mu_3$  bonded glycinate or alaninate moiety, so that all adsorbate–surface complexes are identical (for clarity, we note that there may still be some asymmetry in the precise positions of the donor atoms in the ligand; a description of the footprint as “symmetric” in this instance refers explicitly to the arrangement of the three Cu atoms to which the adsorbate bonds) Those experiments also revealed that, with the onset of  $\mu_2$  bonding at high coverages, other manifestations of chirality emerge in the form of ordered 2D phases that have chiral lattices (alaninate), or of related structures involving highly anisotropic translational domain boundaries, irregularly spaced, whose linear orientation breaks the surface mirror symmetry and whose internal structure is chiral (both glycinate and alaninate).

The behaviour of proline, adsorbed as prolineate  $C_4H_7NHC_2O_2^-$  (Fig. 1b), on Cu{110} exhibits further subtleties. Raval et al. found that prolineate overlayers have a larger unit mesh than glycinate and alaninate overlayers, due to the steric bulk of the pyrrolidine ring containing the

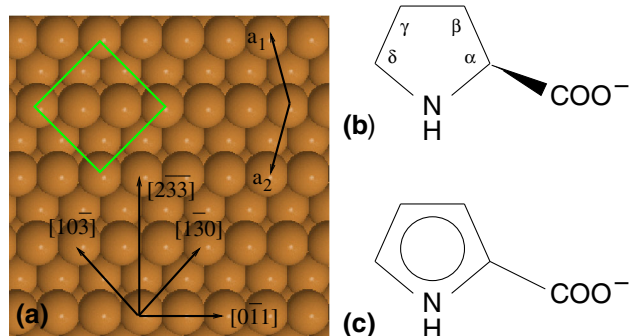


**Fig. 1** **a** Schematic diagram of Cu{311} surface. The choice of basis vectors used to define overlayer matrices is marked, as are key crystallographic directions referred to in the text. The (2,1;1,2) unit mesh is shown in green. **b** L-prolineate; the  $\alpha$ -,  $\beta$ -,  $\gamma$ - and  $\delta$ -C positions are labelled. **c** Pyrrole-2-carboxylate

amine group, and that, for a given molecular enantiomer, the two footprint enantiomers correspond to conformers that place the ring either near-parallel or near-perpendicular, respectively, to the surface plane [32–34]. The same unit mesh and strict alternation of “left-footed” and “right-footed” rows occurs with both enantiopure and racemic prolineate. In the latter case, however, the distribution of D- and L-prolineate (and thus of parallel-ring and perpendicular-ring conformers) is found, within the constraints of the unit mesh and the footprint ordering, to be random.

In light of the structural differences seen in overlayers of prolineate, as compared to glycinate and alaninate, on Cu{110}, we have investigated the structural phases formed when proline is adsorbed on Cu{311}, characterising them by means of reflection–absorption infrared spectroscopy (RAIRS), low-energy electron diffraction (LEED) and scanning tunnelling microscopy (STM). It emerges that the systematics vary significantly from those seen in our earlier investigations of glycine and alanine on Cu{311} [27, 29–31]. We discuss our results for proline in that context, and also in the context of the behaviour of prolineate observed by Raval et al. on Cu{110} [32–34].

## 2 Experimental Details

In common with our previous work, the experiments were performed under ultra-high vacuum (UHV) conditions on single-crystal Cu{311} surfaces [27, 29–31]. The overlayers were prepared by exposing the clean surfaces to gas-phase proline, generated by sublimation from enantiopure L-proline powder in a heated capillary tube; the various exposures used, and the surface temperatures/annealing conditions, were as stated below for specific experiments. The RAIRS and STM measurements were performed in separate UHV systems on two different Cu{311} crystals, as described previously [27, 29–31]; STM images were recorded at 78 K in constant-current (topographic) mode.

LEED measurements were made in both UHV systems, for the purpose of correlating the RAIRS and STM results. The LEED optics in the STM system gives markedly sharper spots and lower background than the optics in the RAIRS system; we have seen this disparity consistently across a range of substrates and adsorbates, and therefore attribute it to instrumental factors, not surface condition. For that reason, the LEED patterns shown here are those recorded in the STM system. LEED measurements were performed at very low energies (typically 23 eV), which are found to minimise electron beam damage to the overlayer.

Although similar trends in the LEED behaviour were observed in both UHV systems, some inconsistencies (discussed explicitly below) were noted in the exposures

and temperatures at which changes occurred in the two systems, as well as some variability in repeated experiments under nominally identical conditions in the same system. In the STM system, saturation was typically achieved at much lower exposures, and with a smaller pressure rise above base pressure, than in the RAIRS system, such that exact exposure values were difficult to assess reliably. This may be due to the fact that there was direct line-of-sight between sample and doser in the STM system but not in the RAIRS system, although we have not investigated this in depth. It is also relevant that the sample heating and temperature measurement arrangements in the two systems are different: in the STM UHV system, the radiatively-heated sample stage in the manipulator has a high thermal mass, and the thermocouple is mounted remotely from the sample plate, making precise temperature control relatively difficult to achieve.

Because of the distortions that arise in STM images due to scanner miscalibration, thermal drift and scanner hysteresis, LEED is more reliable as an accurate guide to surface periodicity. Consequently, in cases where LEED shows a simple periodicity and the corresponding STM images, even if distorted, are clearly consistent, it is justified to use digital processing to correct the STM images to the periodicity determined by LEED. On that basis, high-resolution STM images have been corrected for distortion where possible (“calibrated”, in figure caption). Where the LEED pattern is complex or indistinct, or the correlation with STM less clear, such an approach is less feasible, and the STM data are shown without correction (“uncalibrated”).

To facilitate comparison with LEED data, 2D plots of the power spectra of corresponding STM images were calculated using Image Metrology SPIP software, using a Welch window and displayed using  $\sqrt{(\text{magnitude})}$  scaling. Uncalibrated images were used in all cases: although this inevitably leads to (small) distortions of the power spectrum plots relative to the LEED patterns, any scanner miscalibration is common to all images, so that any inconsistencies between power spectra of different images can be wholly attributed to thermal drift (low on our LT-STM at 78 K) and/or scanner hysteresis.

### 3 Results

#### 3.1 RAIRS and LEED Observations

##### 3.1.1 Development of Prolinate Overlayer with Exposure at 300 K

Figure 2 shows a series of RAIR spectra obtained while exposing Cu{311}, held at 300 K, to L-proline. A key feature is the absorption band at  $1410\text{ cm}^{-1}$ . In common

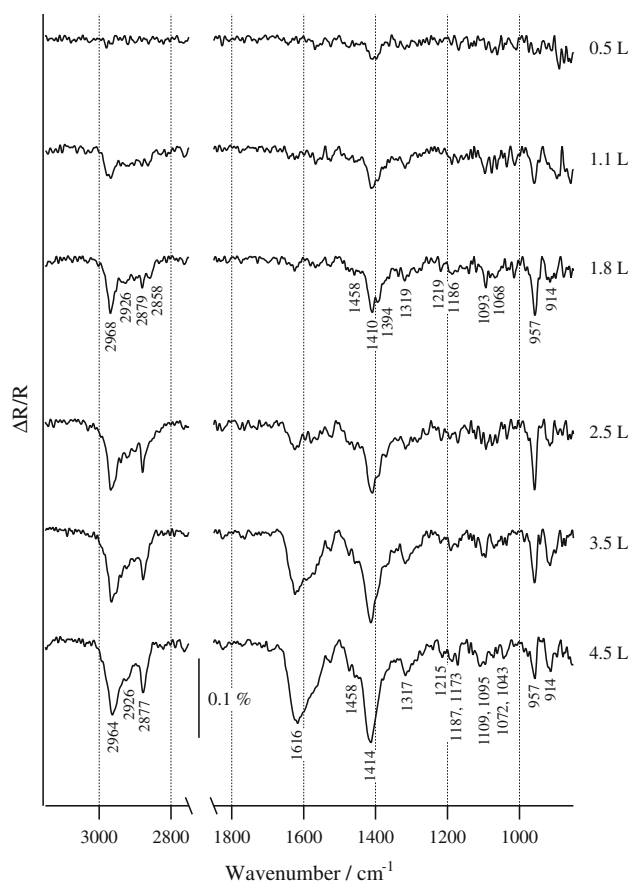


**Fig. 2** RAIR spectra obtained while exposing Cu{311} at 300 K to L-proline

with previous studies [1, 11, 30–32], this is assigned as the symmetric O–C–O stretch,  $\nu_s(\text{CO}_2)$ , and taken as characteristic of the  $\mu 3$  bonding configuration, because it implies that both carboxylate O atoms are in identical environments. This is also the key piece of evidence that the molecule adsorbs in anionic form: the carboxylate O atoms could not be in identical environments if the molecule adsorbed as proline. The strong band at  $957\text{ cm}^{-1}$  is assigned to a stretching mode of the pyrrolidine ring,  $\nu(\text{ring})$ , coupled with the out-of-plane N–H bend,  $\delta(\text{NH})$ ; the weaker band at  $1394\text{ cm}^{-1}$  is assigned to the in-plane N–H bend,  $\delta(\text{NH})$ , coupled to the C–H bend,  $\delta(\text{C}_\alpha\text{H})$ , associated with the  $\alpha$  carbon [32]. The relative strengths of these two bands imply that the N–H bond is close to parallel with the surface, consistent with the amine group bonding to the surface through the N lone pair.

Turning to modes associated with the pyrrolidine ring, the strong band at  $2968\text{ cm}^{-1}$  is assigned to the antisymmetric H–C–H stretch,  $\nu_a(\text{C}_\beta\text{H}_2)$ , associated with the  $\beta$  carbon, coupled to the same mode associated with the  $\gamma$  carbon,  $\nu_a(\text{C}_\gamma\text{H}_2)$ . The weaker band at  $2879\text{ cm}^{-1}$  is assigned to the corresponding symmetric H–C–H stretches,

$\nu_s(\text{C}_\beta\text{H}_2)$  coupled to  $\nu_s(\text{C}_\gamma\text{H}_2)$ , while the weak band at  $2858\text{ cm}^{-1}$  is assigned to the C–H stretch mode,  $\nu(\text{C}_\alpha\text{H})$ , associated with the  $\alpha$  carbon [32]. In principle, the relative strengths of these bands depend in part upon the orientation of the ring relative to the surface plane. However, determining ring orientation on this basis is complicated by the fact that the ring is puckered. We limit ourselves to the observation that the ring is most likely tilted at an orientation intermediate between the two extremes that occur on Cu{110}.

Above 2.5 L exposure, an additional band is seen at  $1616\text{ cm}^{-1}$ . This was originally assigned as the antisymmetric O–C–O stretch,  $\nu_a(\text{CO}_2)$  [1, 11, 32], but has recently been re-assigned, on the basis of ab initio calculations of normal mode frequencies, as a carbonyl stretch,  $\nu(\text{C}=\text{O})$  [30, 31]. On either interpretation, it is characteristic of the  $\mu_2$  bonding configuration, due to the consequent inequivalence of the carboxylate O atoms.

In terms of vibrational spectra, therefore, the behaviour of proline on Cu{311} has clear parallels with the behaviour of glycinate and alaninate on Cu{311} and on Cu{110}, with  $\mu_3$  bonding predominating up to a given coverage, and  $\mu_2$  bonding occurring in addition at higher coverages. But there is also a key difference: with proline, the bands associated with  $\mu_3$  continue to grow while the bands associated with  $\mu_2$  develop.

Figure 3 shows a series of LEED patterns obtained from Cu{311} as a function of exposure to proline at 300 K. These were recorded in the STM UHV system, in which saturation was found to have occurred already at 0.4 L exposure (see below); comparable trends, albeit at systematically higher nominal exposures, were observed in parallel measurements in the RAIRS UHV system. The pattern in Fig. 3b is characteristic of those obtained in the initial stages (up to 0.4 L) of exposure [Fig. 3a shows the clean-surface ( $1 \times 1$ ) LEED pattern for reference]. This pattern can be understood in terms of the (2,1;1,2) overlayer previously observed for glycinate and alaninate on

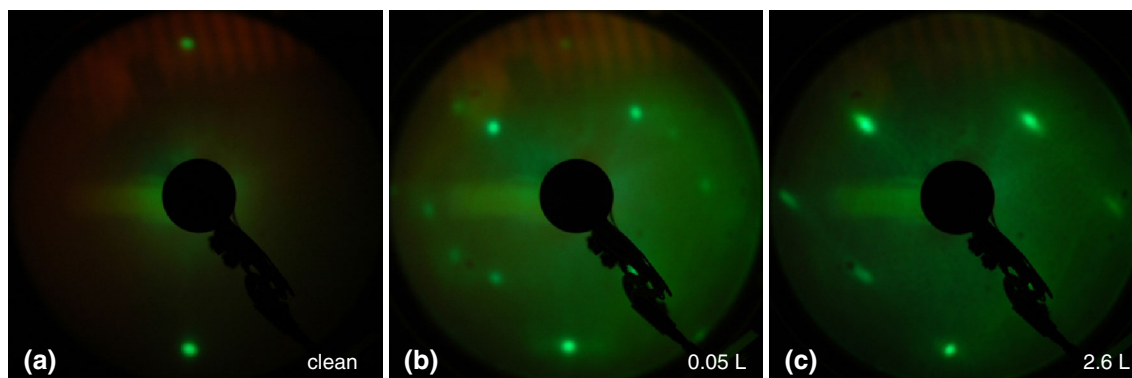
Cu{311} [27, 29–31], but with asymmetric spot-splitting consistent with a slight chiral distortion of the (2,1;1,2) lattice. The pattern in Fig. 3c is characteristic of those obtained at higher exposures (0.4 L and above). This is a (2,1;1,2) LEED pattern, albeit showing slight diagonal elongation of the spots.

The observation of proline overlayers having (2,1;1,2) periodicity on Cu{311} is consistent with the observation of the same periodicity with glycinate and alaninate on Cu{311} [27, 29–31]. In the latter cases, this periodicity is associated with pure  $\mu_3$  bonding in the SL phase at 0.33 ML; at higher exposures, with the onset of  $\mu_2$  bonding, the chiral-lattice (CL) phase is seen instead. With proline, by contrast, the split-spot pattern is seen at lower exposures associated with pure  $\mu_3$  bonding, while the (2,1;1,2) pattern is seen most clearly at higher exposures after the onset of  $\mu_2$  bonding. The systematics for proline evidently differ in detail from those for glycinate and alaninate.

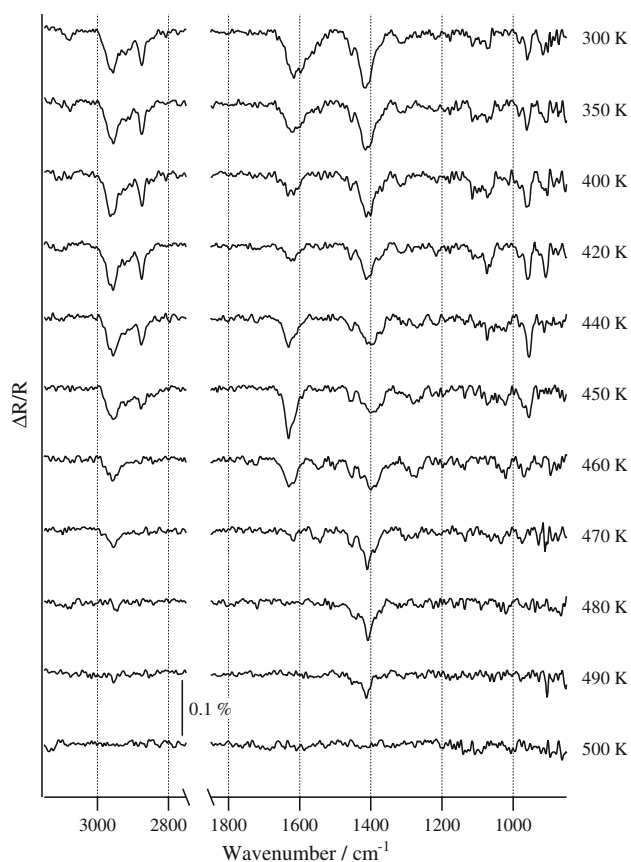
### 3.1.2 Effects of Annealing on Saturated Proline Overlayer

Figure 4 shows how the RAIR spectrum of the saturated surface (after 5 L exposure at 300 K to L-proline) is affected by subsequent annealing. These data were obtained by heating to a given temperature for 2 min, cooling to 300 K and recording a spectrum, heating to the next temperature and so on. We focus in particular on the behaviour of the  $\nu_s(\text{CO}_2)$  and  $\nu(\text{C}=\text{O})$  bands at  $1414$  and  $1616\text{ cm}^{-1}$  respectively.

On annealing to temperatures between 350 and 420 K, the  $\nu_s(\text{CO}_2)$  and  $\nu(\text{C}=\text{O})$  bands both decrease in intensity; the latter also shifts slightly to  $1622\text{ cm}^{-1}$ . These changes could suggest a decrease in the tilt of the carboxylate group relative to the surface plane. From 440 to 450 K, the  $\nu(\text{C}=\text{O})$  band becomes *more* intense, and sharpens, while the  $\nu_s(\text{CO}_2)$  band broadens slightly and shifts to around  $1400\text{ cm}^{-1}$ . This suggests that the tilt of the carboxylate group out of the surface plane increases again. From 460 to



**Fig. 3** LEED patterns recorded from Cu{311} in LT-STM UHV system: **a** clean surface, **b** after 0.05 L exposure at 300 K to L-proline, and **c** after 2.6 L exposure at 300 K to L-proline (all 23 eV)



**Fig. 4** RAIR spectra obtained after exposing Cu{311} at 300 K to 5 L L-proline, followed by annealing to the temperatures shown

480 K, the intensity of the  $\nu(\text{C}=\text{O})$  band decreases progressively to zero, while the  $\nu_s(\text{CO}_2)$  band sharpens and shifts back to  $1410\text{ cm}^{-1}$ . The loss of the  $\nu(\text{C}=\text{O})$  band in particular indicates that no significant quantity of proline remains in the  $\mu_2$  bonding configuration. Other bands decrease in intensity as well, notably the high frequency CH and  $\text{CH}_2$  stretch modes and the ring-stretching band at  $957\text{ cm}^{-1}$ . These observations can plausibly be explained in terms of dehydrogenation of the pyrrolidine ring, triggering aromatisation to give pyrrole-2-carboxylate (Fig. 1c; the alternative explanation, desorption of the overlayer, is discounted for reasons set out below). This explanation is consistent with the observation, in separate temperature programmed desorption (TPD) measurements (Fig. 5) of  $\text{H}_2$  desorption between 450 and 530 K, with a maximum at 490 K (hydrogen is unstable on the surface at these temperatures). The  $\nu_s(\text{CO}_2)$  band—the only substantial band remaining at this point—in turn disappears progressively on annealing between 490 and 500 K, leaving a featureless RAIR spectrum.

These trends again show significant differences compared to those observed on annealing alaninate or glycinate overlayers on Cu{311}. In those cases, peaks related to  $\mu_2$

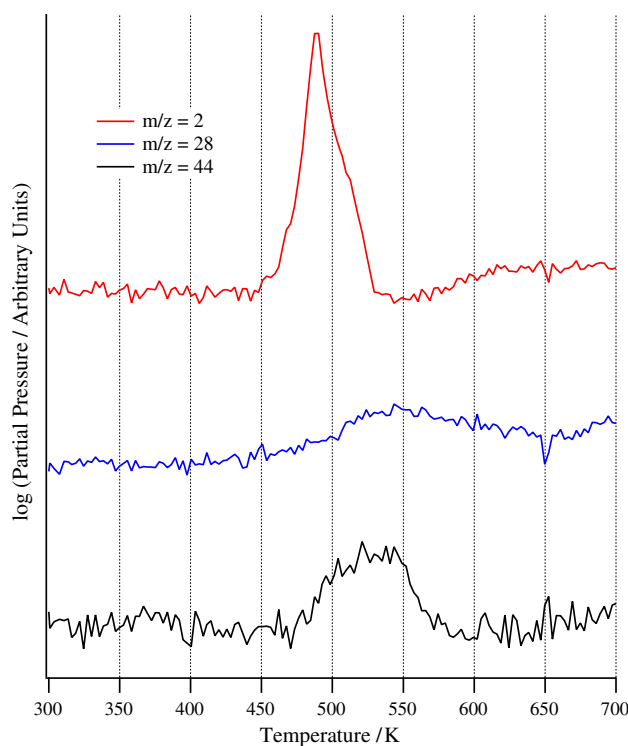


**Fig. 5** TPD profiles recorded after exposing Cu{311} at 300 K to 7.5 L of L-proline. Heating rate:  $0.5\text{ K s}^{-1}$

bonding decrease progressively on heating, indicating a reversion to pure  $\mu_3$  bonding by 460 K; bands associated with the latter disappear in turn by 480 K (glycinate)/490 K (alaninate) [27, 29–31].

Figure 6 shows a series of LEED patterns obtained after saturation exposure at 300 K to L-proline, followed by progressive annealing steps. The LEED pattern obtained after an initial 0.4 L exposure (Fig. 6a) is similar to that obtained after 2.6 L exposure (Fig. 3c) indicating that  $<0.4\text{ L}$  exposure is sufficient to obtain the saturation structure in the STM UHV system. This inference is reinforced by the observation that similar sequences of LEED patterns were obtained in the RAIRS UHV system after 5 L initial exposure. On annealing up to 400 K, a slight diagonal streaking of the spots, seen after initial deposition, is lost, giving a sharp (2,1;1,2) pattern. From 420 to 460 K, a faint secondary set of spots is visible: we show below that this can be understood in terms of spot-splitting due to mesoscopic-scale periodic ordering. A slight clockwise azimuthal twist of the split pairs, which can be seen at 420 K, disappears at 460 K to give symmetric splitting. After annealing to 470–480 K, the splitting disappears, leaving a faint, diffuse (2,1;1,2) pattern and a high background indicative of substantial disorder. From 480 to 490 K, the (2,1;1,2) pattern is replaced by a different set of fractional order spots. These are diffuse with a high background after annealing at 480 K, but sharpen at 490 K

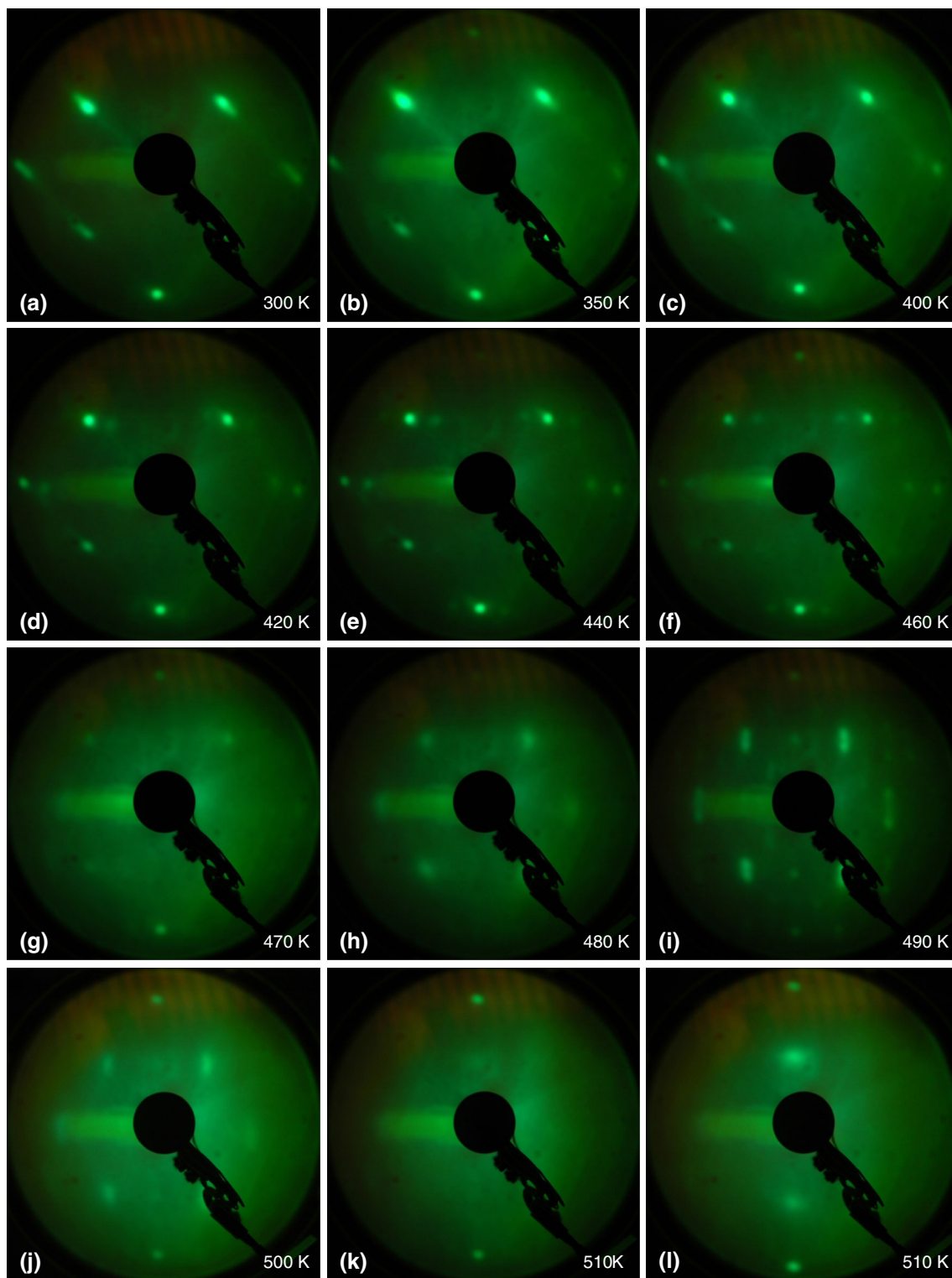
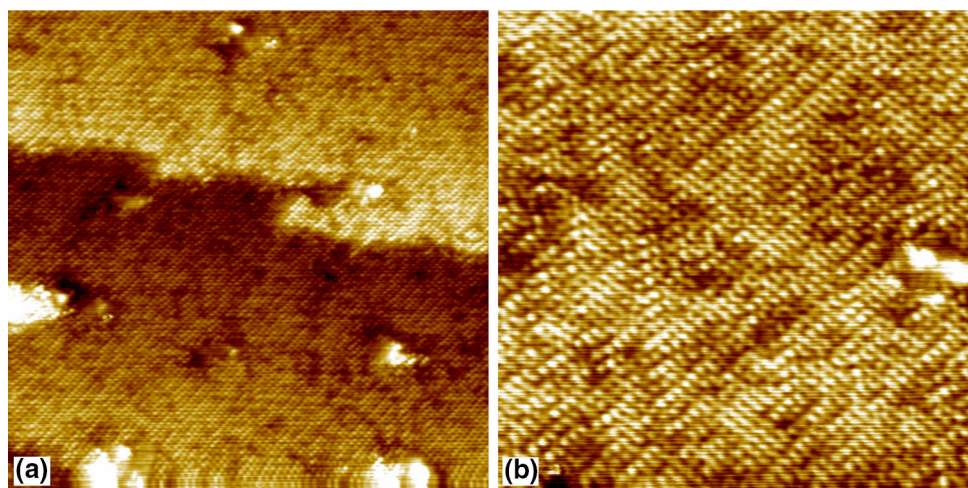


**Fig. 6** LEED patterns recorded from Cu{311} in LT-STM UHV system after saturation exposures (0.4 L, **a–i**; 2.5 L, **j–l** in a separate experiment) to L-proline at 300 K, followed by annealing in stages to temperatures shown (2 min each) (all 23 eV, recorded at 300 K)

to give a new pattern which we identify in Sect. 3.2.2 as corresponding to a coincidence net structure, comprising two domains described by  $(2.5, 1.5; 2, 3)$  and  $(3, 2; 1.5, 2.5)$

matrices. This pattern fades in turn at 500 K, leaving just integer-order spots at 510 K—although diffuse half-order spots become visible at 19 eV beam energy (Fig. 6l).

**Fig. 7** Constant-current STM images of Cu{311} after exposure to 0.05 L of L-proline at 300 K. **a**  $500 \times 500 \text{ \AA}^2$ , tip bias voltage +1.0 V, tunnelling current 0.50 nA, uncalibrated. **b**  $200 \times 200 \text{ \AA}^2$ , showing imperfectly ordered (2,1;1,2)-based structure; +10 mV, tunnelling current 20 pA, uncalibrated



This sequence of LEED patterns is distinct from those seen with glycinate and alaninate on Cu{311}. In the latter cases, reversion of the RAIR spectrum to pure  $\mu_3$  bonding correlates with reversion of the LEED pattern to (2,1;1,2) [27, 29–31]. Here, the clearest (2,1;1,2) LEED pattern occurs under high-exposure conditions where RAIRS indicates mixed  $\mu_3$  and  $\mu_2$  bonding. The sequence of changes in the streaking and spot-splitting of LEED patterns recorded after annealing to temperatures between 350 and 460 K appears to correlate with the sequence of changes seen in the intensity of the  $\nu(\text{C=O})$  and  $\nu_s(\text{CO}_2)$  bands in this temperature range. More clearly, the loss of the (2,1;1,2) LEED pattern and emergence of the coincidence net structure at 480–490 K coincide with changes in the RAIRS that we have tentatively attributed to aromatization of the pyrrolidine ring. We discuss this possibility in more detail below.

### 3.2 STM Structural Observations

#### 3.2.1 Prolinate Structural Phases

In order to gain more detailed insights into the structural characteristics of these proline-derived overlayers, STM measurements were made following preparation conditions corresponding to the most characteristic LEED patterns.

Figure 7 shows representative images of Cu{311} after a sub-saturation exposure (0.05 L) to L-proline at 300 K, corresponding to the LEED pattern in Fig. 3b. The larger-area image (Fig. 7a) shows a slightly patchy appearance to the terraces, occasional pits and clusters, and an irregular step whose orientation is ill-defined. The high-resolution image (Fig. 7b) reveals that the molecular overlayer is imperfectly ordered, with regular ordering in the  $[10\bar{3}]$  direction, but significantly less regular ordering in the  $[1\bar{3}0]$  direction, with clear termination, and/or deviation in

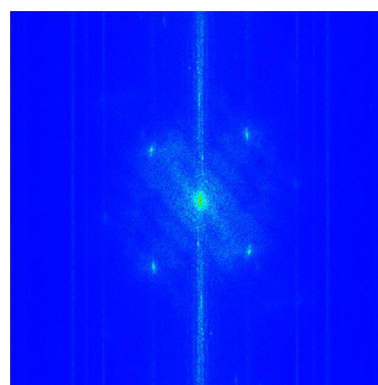


**Fig. 8** Power spectrum of image in Fig. 7a

direction, of individual rows. Brighter patches are typically consistent with approximately (2,1;1,2) periodicity (see later); some breakdown of the 2D periodic order is particularly apparent in the darker patches. Qualitatively, there is also some suggestion of ‘banding’, with bands running in the  $[1\bar{3}0]$  direction.

Figure 8 shows the power spectrum of the STM image in Fig. 7a. This reproduces the principal features of the LEED pattern well: in particular, the marked skewing of the reciprocal mesh away from that expected for ideal (2,1;1,2) periodicity matches well with the asymmetric spot-splitting in the LEED. The STM and LEED data are thus at least qualitatively consistent: there is evidence of distorted (2,1;1,2) periodicity in both, with the spot-splitting, and direction thereof, in the LEED pattern consistent with the banding seen in STM images. Because these data correspond to conditions in which RAIR spectra indicate pure  $\mu_3$  bonding, the implication is that at 300 K, prolinate can self-assemble into locally (2,1;1,2)-like regions, but some kinetic barrier (perhaps associated with the bulk of the pyrrolidine rings) precludes perfect (2,1;1,2) ordering, such that some residual disorder remains in the overlayer.

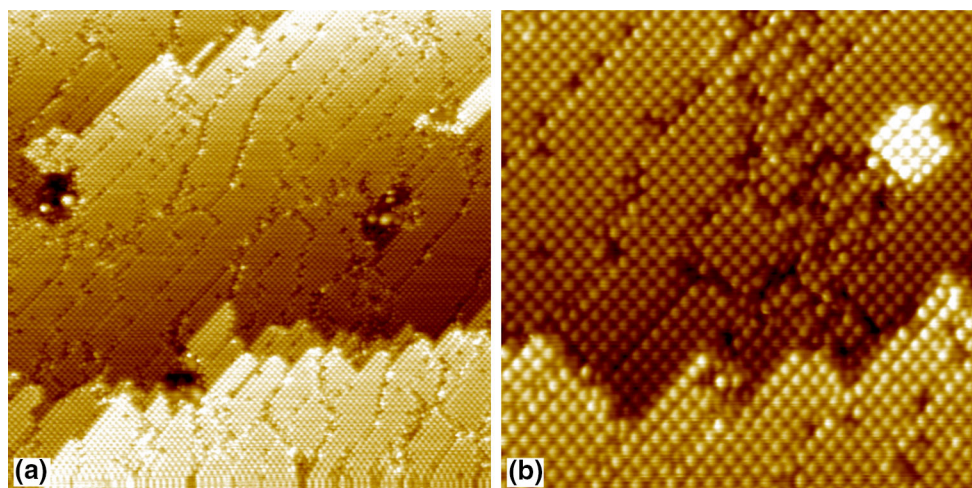


**Fig. 9** Constant-current STM images of Cu{311} after exposure to 3 L of L-proline at 300 K, and annealing to 350 K. **a**  $500 \times 500 \text{ \AA}^2$ , +1.0 V, 1.0 nA, uncalibrated. **b**  $200 \times 200 \text{ \AA}^2$ , showing domains of

(2,1;1,2) overlayer, punctuated by various kinds of boundary; +0.1 V, 50 pA, calibrated

Figure 9 shows representative images of Cu{311} after saturation exposure (3 L) to L-proline at 300 K, followed by annealing to 350 K. The corresponding LEED pattern, identical to Fig. 6b, indicates (2,1;1,2) overlayer periodicity, and this is confirmed by the STM measurements. Figure 9a shows the overall morphology: the terraces exhibit (2,1;1,2) periodicity, punctuated by a variety of linear and approximately linear features running predominantly in the  $[1\bar{3}0]$  direction defined by one of the sides of the (2,1;1,2) unit mesh, as well as occasional islands and pits. Steps now show pronounced faceting, with clear alignment in the  $[1\bar{3}0]$  direction, and some degree of alignment in the  $[10\bar{3}]$  direction: these directions correspond to the sides of the (2,1;1,2) unit mesh. The power spectrum of this image (Fig. 10) satisfactorily reproduces the (2,1;1,2) LEED pattern, including the asymmetric streaking due to the irregular spacing of the  $[1\bar{3}0]$  linear features (the slight residual skewing of the reciprocal mesh can be attributed in this case to scanner miscalibration etc.). The high-resolution image (Fig. 9b) shows the structural features in detail. The linear features represent boundaries between well-ordered (2,1;1,2) regions: they run predominantly in the  $[1\bar{3}0]$  direction and have a characteristic internal structure; in places, the orientation varies, and the internal structure is less well defined. One extended boundary region is visible (top centre), in which a few repeats of a clearly-defined larger unit mesh structure, with (4,2;2,4) periodicity and involving zig-zag  $[1\bar{3}0]$  rows, can be seen.

The linear  $[1\bar{3}0]$  boundaries are strongly reminiscent of similar features observed for glycinate and alaninate on Cu{311} [27, 29, 30]; in all cases, they are seen after preparation conditions corresponding to the onset of  $\mu_2$  bonding. However, we note some important differences.

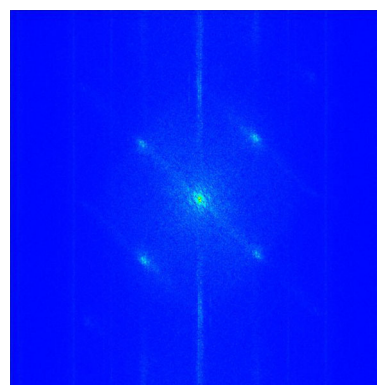


**Fig. 10** Power spectrum of image in Fig. 9a

The first is in the correlation between structure and bonding configuration. For proline, (2,1;1,2) periodicity appears to be associated with mixed  $\mu_3$  and  $\mu_2$  bonding. For glycinate and alaninate, however, (2,1;1,2) periodicity is associated with pure  $\mu_3$  bonding, whereas the onset of  $\mu_2$  bonding is linked to boundaries and/or ordered CL structures and corresponding changes in the LEED pattern. The second difference is that, whereas the boundaries seen with glycinate and alaninate are translational domain boundaries, those seen in these proline images are not: adsorbates in the (2,1;1,2) regions either side of the boundary sit on the same lattice, and the adjacent (2,1;1,2) regions are thus in the same translational domain. In consequence, the internal structure (or structures) of the  $[1\bar{3}0]$  boundaries seen for proline is unlike that of the boundaries seen for glycinate and alaninate. Similarly, the deviations from  $[1\bar{3}0]$  orientation seen for proline are not seen for glycinate and alaninate.



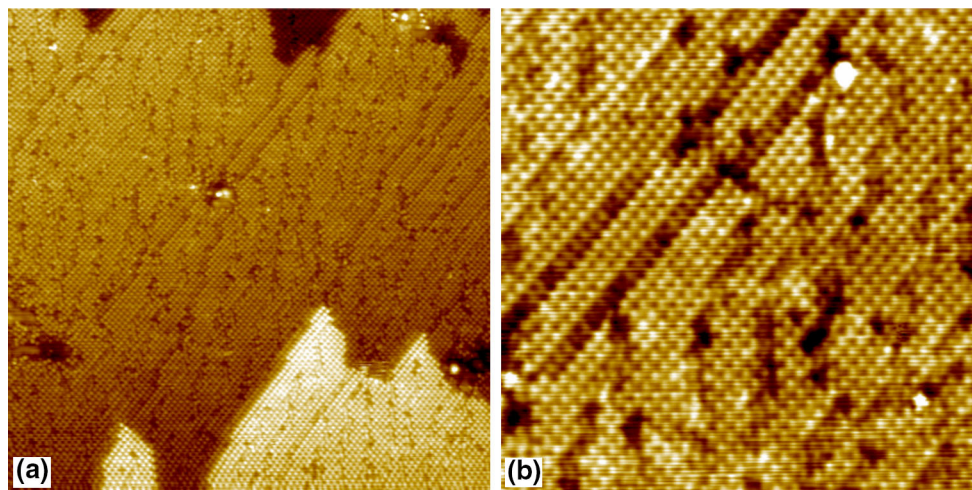


**Fig. 11** Constant-current STM images of Cu{311} after exposure to 0.4 L of L-proline at 300 K, and annealing to 460 K. **a**  $500 \times 500 \text{ \AA}^2$ , +1.0 V, 1.0 nA, uncalibrated. **b**  $200 \times 200 \text{ \AA}^2$ , showing domains of

(2,1;1,2) overlayer, punctuated by various kinds of boundary; +1.0 V, 1.0 nA, calibrated

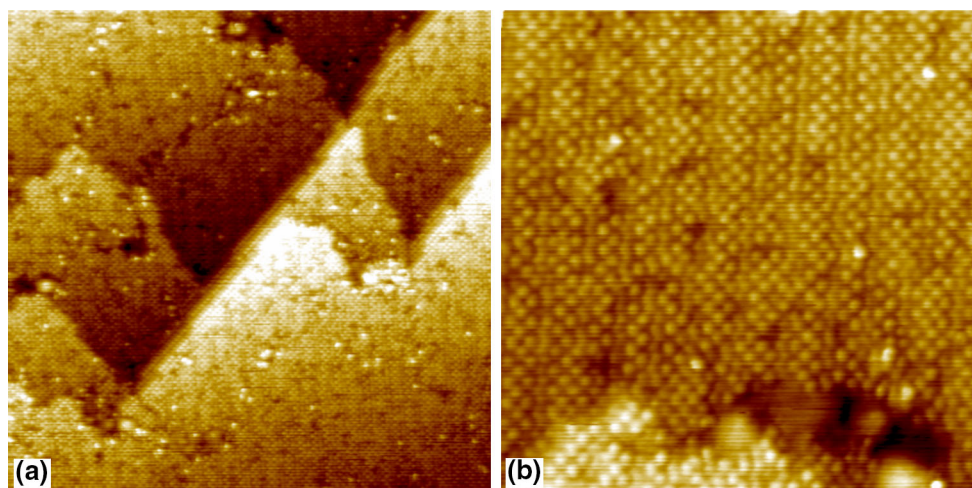


**Fig. 12** Constant-current STM images of Cu{311} after exposure to 2.5 L of L-proline at 300 K, and annealing to 480 K. **a**  $500 \times 500 \text{ \AA}^2$ , +1.0 V, 0.2 nA, uncalibrated. **b**  $200 \times 200 \text{ \AA}^2$ , showing narrow

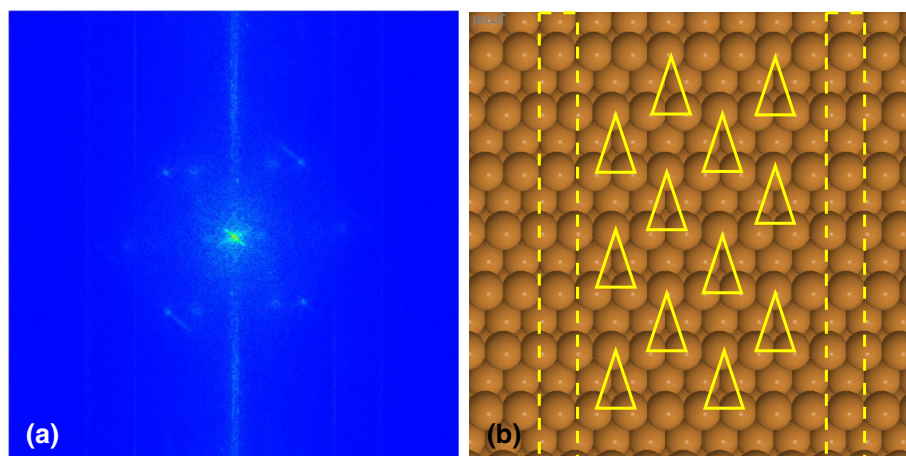
domains of (2,1;1,2) overlayer, punctuated by  $[2\bar{3}\bar{3}]$  boundaries, +0.1 V, 10 pA, calibrated

Figure 11 shows representative images of Cu{311} after saturation exposure (0.4 L) to L-proline at 300 K, followed by annealing to 460 K. The corresponding LEED pattern (Fig. 6f) shows a symmetric split-spot (2,1;1,2) pattern. Figure 11a shows the overall morphology: terraces again exhibit (2,1;1,2) periodicity, punctuated by boundaries. Step alignment in the  $[1\bar{3}0]$  direction is still evident, although there seems to be less of a tendency for alignment in the  $[10\bar{3}]$  direction. This image also reveals another important feature: a change in the average alignment of the mid-terrace boundaries away from  $[1\bar{3}0]$  (as seen in Fig. 9) towards  $[2\bar{3}\bar{3}]$ ; boundaries also appear to account for a higher fraction of the surface area. At higher resolution (Fig. 11b) short lengths of a characteristic boundary

running in the  $[2\bar{3}\bar{3}]$  direction can be seen: the internal structure is difficult to discern, but the  $[2\bar{3}\bar{3}]$  termination of the adjacent (2,1;1,2) domains is clear. The internal structure of the  $[1\bar{3}0]$  boundaries also appears different from that seen in Fig. 9b. Although the differences may in part be due to a different tip condition, the boundaries do appear less internally constricted.

Figure 12 shows representative images of Cu{311} after saturation exposure (2.5 L) to L-proline at 300 K, followed by annealing to 480 K. In general, LEED patterns obtained after annealing to 470–480 K showed a diffuse (2,1;1,2) pattern (Fig. 6g) or no LEED pattern at all. The specific surface preparation from which these STM images were obtained was one of those which showed no LEED pattern

**Fig. 13** **a** Power spectrum of image in Fig. 12a. **b** Schematic showing approximate domain width indicated by spot splitting. *Yellow triangles* represent  $\mu_3$  proline bonding footprint; *dashed rectangles* represent domain boundaries



at all. Such a disparity between the LEED and STM data is very surprising: we are unable to account for this, and believe it to be anomalous. The overall morphology (Fig. 12a) is broadly similar to that seen in Fig. 11a, but with less clear definition of the step faceting, and some indications of greater disorder on the terraces (bright adfeatures, pits). Significant changes can be seen in the high-resolution image (Fig. 12b): the terraces now exhibit extended  $[2\bar{3}\bar{3}]$  boundaries, relatively regularly spaced (around 15 Å), separating narrow domains of the (2,1;1,2) structure. No remnant of the  $[1\bar{3}0]$  boundaries remains.

Figure 13a shows the power spectrum of the STM image in Fig. 12a: it matches very closely with the symmetric split-spot LEED pattern shown in Fig. 6f. To the precision with which it can be measured in the LEED pattern or the power spectrum, this symmetric splitting corresponds to a real space periodicity between 7 and 9 lattice spacings in the close-packed direction. Given the finite width of the boundaries, the width of the intervening (2,1;1,2) domain should be 3–4  $[2\bar{3}\bar{3}]$  rows, shown schematically in Fig. 13b. This correlates very well with the average domain width observed in the high-resolution STM image (Fig. 12b).

Overall, therefore, there is good correlation between the sequence of changes observed in the LEED and STM data between 350 and 480 K, and these changes evidently correspond to the sequence of changes seen, most notably in the  $\nu(\text{C}=\text{O})$  and  $\nu_s(\text{CO}_2)$  bands, in the RAIR spectra over the same temperature range. However, some discrepancies exist in the detailed correlation of STM and LEED data in the approximate temperature range 420–480 K. In particular, the apparent *average* boundary orientation seen after a 460 K anneal in the STM (Fig. 11) is not entirely consistent with the degree of azimuthal twist of the split spots in LEED patterns between 420 and 460 K, and—as already remarked—the STM data obtained after a 480 K anneal (Fig. 12) corresponds best to the LEED pattern obtained after a 460 K anneal (Fig. 6f) rather than a 470 or

480 K anneal (Fig. 6g, h). At present, we cannot account for these discrepancies.

### 3.2.2 Proline-Derived Structural Phases After High-Temperature Annealing

Figure 14 shows representative images of Cu{311} after saturation exposure (0.4 L) to L-proline at 300 K followed by annealing to 490 K, corresponding to the LEED pattern in Fig. 6i. Much of the terrace shown in Fig. 14a is covered by ill-defined, amorphous clusters of varying sizes. However, a periodically ordered structural phase can be seen underlying the amorphous layer. Figure 14b shows a region of the surface in which a relatively large area of the ordered phase is exposed. Two domains are visible, one clearly the mirror image of the other (the mirror plane runs vertically down the image, consistent with the Cu{311} surface mirror symmetry), with a domain boundary running horizontally across the image approximately a quarter of the way from the top (arrowed “B”). Within each domain, adsorbates define a distorted hexagonal grid, the distortion breaking the mirror symmetry of the substrate: the corresponding 2D lattice is therefore chiral. In a number of regions, a subset of adsorbates image brighter, locally defining a “(2 × 2) super-mesh” of the basic overlayer periodicity.

Figure 15 shows the power spectrum of the STM image in Fig. 14a. The clearest fractional-order peaks are fully consistent with the dominant spots in the LEED pattern shown in Fig. 6i. Careful analysis of the reciprocal meshes defined by the dominant peaks in the power spectrum (or equivalent analysis of the corresponding LEED spots) allows the real-space unit meshes of the two overlayer domains to be determined as having periodicities (2.5,1.5;2,3) and (3,2;1.5,2.5): the schematic LEED pattern in Fig. 16 shows the fractional-order spots expected for this periodicity (filled circles), demonstrating perfect agreement with

**Fig. 14** Constant-current STM images of Cu{311} after exposure to 0.4 L of L-proline at 300 K, and annealing to 490 K. **a**  $500 \times 500 \text{ \AA}^2$ ,  $-0.1 \text{ V}$ ,  $50 \text{ pA}$ , uncalibrated. **b**  $200 \times 200 \text{ \AA}^2$ , showing two domains of  $(2.5, 1.5; 2, 3)$  structure;  $+0.1 \text{ V}$ ,  $50 \text{ pA}$ , uncalibrated

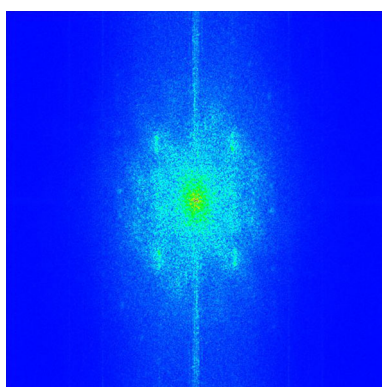
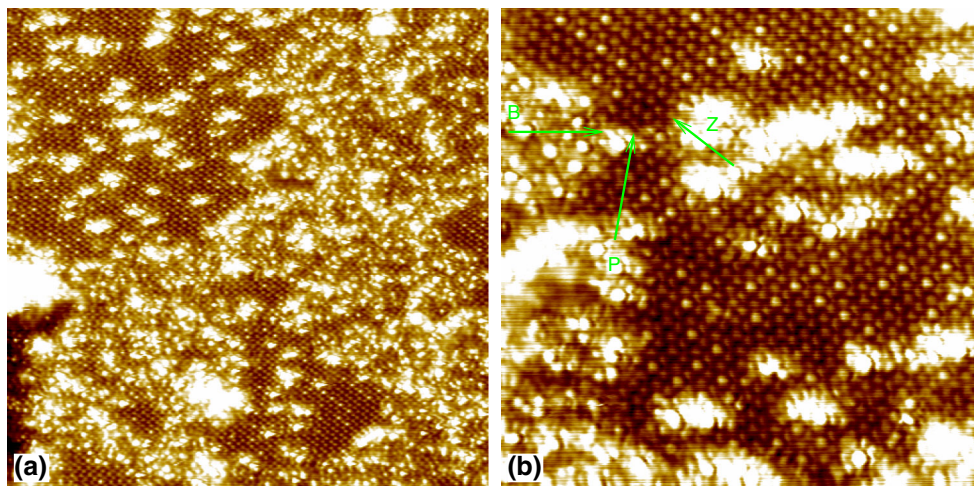
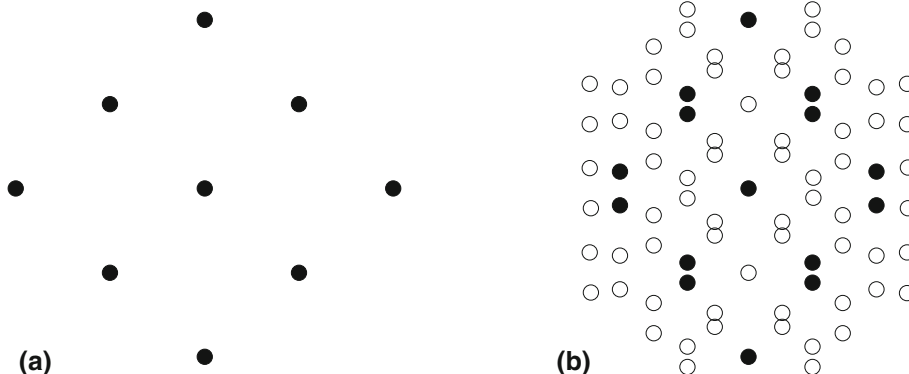


**Fig. 15** Power spectrum of image in Fig. 14a

the LEED pattern and the power spectrum of the STM image. The rational-fraction matrix elements show that the full surface structure is a coincidence net structure. We defer a detailed discussion of this overlayer structure to Sect. 4.

Finally, Fig. 17 shows representative images of Cu{311} after saturation exposure (2.5 L) to L-proline at 300 K followed by annealing to 510 K, corresponding to

**Fig. 16** Schematics illustrating, at the same scale, LEED patterns expected for **a** the  $(2, 1; 1, 2)$  net (central column of spots are integer-order), and **b** both mirror domains of the  $(2.5, 1.5; 2, 3)$  net (filled circles) and the  $(5, 3; 4, 6)$  net (open circles)



the LEED patterns in Fig. 6k, l. The step faceting seen in images of proline overlayers has been lost (Fig. 17a), and there is a high incidence of clusters and pits. At higher magnification (Fig. 17b) a layer of molecular-scale features can still be seen underlying the clusters, but with little or no periodic order visible. This is consistent with the absence of fractional-order spots in the 23 eV LEED pattern (Fig. 6k); there is nothing in the STM image to indicate the origin of the half-order spots in the 19 eV LEED pattern (Fig. 6l). These images show that complete desorption of all proline-derived species has *not* occurred. Given the absence of absorption bands in the corresponding RAIR spectrum, the inference must be that further fragmentation has instead occurred, leading to species/orientations that are not RAIRS-active.

#### 4 Discussion

From these results, we see that there are two clear points of similarity in the behaviour of proline, alaninate and glycinate on Cu{311} observed in this and our previous

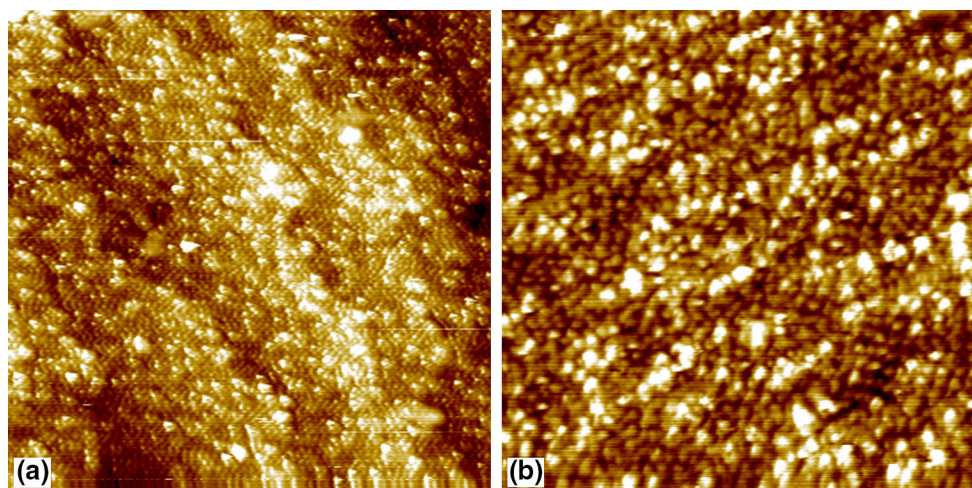


**Fig. 17** Constant-current STM images of Cu{311} after exposure to 2.5 L of L-proline at 300 K, and annealing to 510 K. **a**  $500 \times 500 \text{ \AA}^2$ , +0.1 V, 0.1 nA, uncalibrated. **b**  $200 \times 200 \text{ \AA}^2$ , showing residual

molecular species after dissociation of previous species; +10 mV, 10 pA, uncalibrated

studies [27, 29–31]. The first is the transition from pure  $\mu_3$  bonding to a mixture of  $\mu_3$  and  $\mu_2$  bonding with increasing exposure, and the loss of  $\mu_2$  bonding on annealing. The second is the observation of (2,1;1,2) periodicity. However, there are also several notable differences: (i) the continued growth in the RAIR spectra of absorption bands associated with  $\mu_3$  bonding after the onset of  $\mu_2$  bonding; (ii) the detailed behaviour of the  $\nu(\text{C}=\text{O})$  and  $\nu_s(\text{CO}_2)$  bands on annealing; (iii) the relationship between (2,1;1,2) periodicity and  $\mu_3/\mu_2$  bonding behaviour; (iv) the nature and behaviour of the ‘domain boundaries’, and their relationship to  $\mu_2$  bonding; (v) the high-temperature structures.

The presence in the RAIR spectra of absorption bands associated with  $\mu_3$  bonding, and the observation of a (2,1;1,2) LEED pattern, strongly imply that proline, alaninate and glycinate share essentially the same symmetric bonding footprint (in terms of Cu atom positions) on Cu{311}. Given the coexistence of bands associated with  $\mu_2$  bonding, however, we cannot rule out the possibility that the distinction between  $\mu_3$  and  $\mu_2$  bonding becomes blurred in this case. The lower conformational flexibility, compared to alaninate/glycinate, imposed by the pyrrolidine ring may introduce some asymmetry into the bonding of the two carboxylate O atoms to the surface. Nevertheless,  $\mu_2$  bonding remains most strongly associated with higher exposures, whereas at lower exposures, when RAIR spectra show pure  $\mu_3$  bonding, LEED and STM data indicate that (2,1;1,2) periodicity is only imperfectly established. This can most obviously be attributed to the steric bulk of the pyrrolidine ring impeding the ordering process, such that higher coverages are needed to force local order.

The single H atom in the amine group of proline means that there is less scope, compared to alaninate and glycinate, for H-bonding interactions. The fact that the same (2,1;1,2)

periodicity is seen for all three species therefore suggests that H-bonding is not the dominant driving force for this ordering (otherwise one might expect proline overlayers to adopt a different periodicity), the periodicity instead being governed by packing considerations and the bonding footprint. Nevertheless, the marked step faceting behaviour observed after moderate annealing, whereby the step orientation aligns with the edges of the (2,1;1,2) overlayer mesh, suggests that the steps may be stabilised to some extent by H-bonding interactions between neighbouring adsorbates along the down-step edge.

On Cu{110}, the  $(4 \times 2)$  periodicity adopted by  $\mu_3$ -bonded proline is larger, due to the steric bulk of the pyrrolidine ring, than the  $(3 \times 2)$  periodicity adopted by alaninate and glycinate. This leads to a corresponding difference in the ordering of the footprints which underlies the conformer-ordering phenomena noted by Raval et al. [33, 34]. Our results indicate that no such differences occur on {311}, all three adsorbates giving the same (2,1;1,2) periodicity and essentially identical adsorbate–substrate bonding configurations, because the larger row–row spacing of Cu{311} relative to {110} is able to accommodate bulkier species. Note that in RAIR spectra obtained from Cu{110} at high proline exposures, the  $\nu(\text{C}=\text{O})$  absorption band characteristic of  $\mu_2$  bonding is much weaker than it is in spectra obtained from Cu{311}, consistent with the absence of higher-coverage structural phases beyond  $(4 \times 2)$  [33].

For glycinate and alaninate on Cu{311}, the onset of  $\mu_2$  bonding is clearly linked to the presence of translational domain boundaries and/or ordered CL structural phases [27, 29–31]. The rationale is simple: pure  $\mu_3$  bonding at 0.33 ML coverage accounts for all surface-layer Cu atoms in bonding interactions with amine groups or carboxylate O atoms. To increase the coverage beyond this point, it is

necessary for some of the already-adsorbed moieties to convert from  $\mu_3$  to  $\mu_2$  bonding, to free up Cu atoms for ( $\mu_2$ ) bonding to additional adsorbates. Although the details of the boundary structure and of high-coverage structures remain to be determined, they clearly must contain  $\mu_2$ -bonded glycinate/alaninate.

This simple rationale seems to break down somewhat in the case of proline on Cu{311}—although we note an analogous discrepancy on Cu{110}, in that the onset of  $\mu_2$  bonding of glycinate has not been reported as leading to the structural changes away from the  $(3 \times 2)$  phase that are observed with the onset of  $\mu_2$  bonding of alaninate. The characteristic  $[1\bar{3}0]$  boundary orientation is common to L-proline and L-alaninate on Cu{311}, and is also seen (together with mirror-equivalent  $[10\bar{3}]$ -oriented boundaries) with glycinate; this preferred orientation, parallel to one of the sides of the  $(2,1;1,2)$  unit mesh, can be attributed to the same inter-adsorbate H-bonding interactions that stabilise the  $(2,1;1,2)$  periodicity and the  $[1\bar{3}0]$  step facet direction. However, the detailed structure of the proline boundaries is different from that seen with alaninate and glycinate [27, 29, 30]; indeed the proline boundary structure seems to differ between Figs. 9 and 11. Moreover, whereas the boundaries seen with glycinate and proline are translational domain boundaries, those seen with proline appear to separate adjacent regions of the same translational domain.

A conceivable explanation lies in the bulk of the pyrrolidine rings: packing these at 0.33 ML coverage may give rise to higher levels of compressive surface stress than occurs with the smaller amino acids at the same coverage. If so, boundaries may arise in order to relieve excessive levels of stress associated with larger domains (as seen, for example, in N overlayers on Cu{100} [35–38]), in which case these features may be regarded as a form of Frenkel–Kontorova boundary [39]. That picture does not immediately explain the presence or identity of adsorbates within the boundary, however, although the packing density of these moieties does appear to be less than applies in the  $(2,1;1,2)$  phase, in that sites within the boundary are not fully populated. The exact relationship between boundary structure(s) and bonding configuration(s) for proline, and how these relate to the translational domain boundaries seen for alaninate and glycinate, therefore remains unclear at present.

Where the behaviour of proline clearly differs from that of alaninate and glycinate on Cu{311} is in the progressive change of boundary orientation, from  $[1\bar{3}0]$  towards  $[2\bar{3}\bar{3}]$ , with annealing. The internal structure of the  $[2\bar{3}\bar{3}]$  boundaries is indistinct in the STM images; the clear resolution of the adjacent  $(2,1;1,2)$  domains indicates that this indistinctness is somehow related to the structure, rather than to tip effects etc. With the caveats about temperature discrepancies noted above, these structural

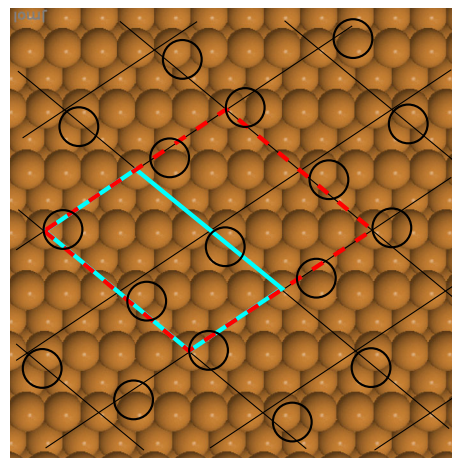


**Fig. 18** Schematic showing periodicities associated with overlayer structure after annealing to 490 K. *Black lines* define a  $(2.5, 1.5; 2, 3)$  net. The  $(5, 3; 2, 3)$  unit mesh is shown in *blue*, the  $(5, 3; 4, 6)$  mesh [or “ $(2 \times 2)$  super-mesh”] in *red*. *Open circles* indicate the pattern of lateral displacements seen in STM images, with an arbitrary registry (see text) placing apical moieties in short bridge positions

changes correlate with the changes seen in the  $\nu(\text{C}=\text{O})$  absorption band in the RAIR spectrum—changes not seen for alaninate or glycinate. The presence of  $(2,1;1,2)$  domains, associated with (predominantly)  $\mu_3$  bonding, adjacent to these boundaries is consistent with the coexistence in the spectra of bands corresponding to  $\mu_3$  bonding.

Perhaps the most striking difference seen with proline, as compared to glycine and alanine, on Cu{311} is the new structural phase formed after annealing to 490 K. Figure 18 shows, superposed on a ball model of the Cu{311} surface, the  $(2.5, 1.5; 2, 3)$  net of one of the two overlayer domains (that visible at the top of Fig. 14b) determined from the LEED pattern and the power spectrum of the STM data. It is clear from this diagram that the full periodicity of the coincidence net should be defined by the matrix  $(5, 3; 2, 3)$ , i.e. twice the size of the  $(2.5, 1.5; 2, 3)$  overlayer net.

No obvious evidence of this  $(5, 3; 2, 3)$  coincidence net periodicity is visible in the STM image. However, the prominent subset of features that image extra-bright define an incomplete “ $(2 \times 2)$  super-mesh” of the  $(2.5, 1.5; 2, 3)$  net, formally described by a  $(5, 3; 4, 6)$  matrix (Fig. 18). Moreover, close inspection of the ordered structure in the STM image reveals a systematic pattern of lateral displacements, leading to marked pairing along rows in the direction marked by arrow P, and zig-zagging of alternate rows running in the direction marked by arrow Z. The nominal molecular positions indicated by the STM data are shown schematically (with arbitrary registry to the substrate) in Fig. 18. The periodicity defined by these displacements is again  $(5, 3; 4, 6)$ . Close inspection of the LEED pattern in Fig. 6i reveals additional faint spots between the dominant spots of the  $(2.5, 1.5; 2, 3)$  periodicity.

These faint spots correspond to a (5,3;4,6)—but *not* a (5,3;2,3)—net, as shown schematically for comparison in Fig. 14b; in other words, the full LEED pattern is consistent with the (5,3;4,6) periodicity seen by STM. In the STM image, both the incompleteness of the “(2 × 2) supermesh” of extra-bright features, and the subtlety of the (5,3;4,6) pattern of lateral displacements, are consistent with the faintness of these additional spots of the full (5,3;4,6) LEED (with the caveat that the LEED patterns were recorded at a single energy).

In Sect. 3.1.2, we advanced the suggestion, based on RAIRS and TPD evidence of dehydrogenation of the pyrrolidine ring, that the surface species at this point may be pyrrole-2-carboxylate (Fig. 1c). One would expect this species to bond to the surface through the carboxylate group and through the molecular  $\pi$  system, and thus to lie substantially parallel to the surface. In this orientation, vibrational modes associated with the backbone and ring should be close to RAIRS-inactive, accounting for the absence of the associated bands in the spectrum. The carboxylate group itself must remain tilted away from the surface, to account for the sole remaining spectral feature, the  $\nu_s(\text{CO}_2)$  absorption band. It is beyond the scope of these data to indicate whether the molecule is planar and slightly tilted out of the surface plane, or whether the backbone bends such that the pyrrole ring is parallel to the surface while the carboxylate group is tilted.

The (5,3;4,6) periodicity, with four moieties visible per unit mesh, implies a surface coverage of 0.22 ML, substantially less than the 0.33 ML coverage of (2,1;1,2) proline. This is consistent with the observation of a substantial amount of amorphous material—which may be the excess 0.11 ML of pyrrole-2-carboxylate that cannot be accommodated in the first layer, or may be further dissociation products—above the ordered layer. This reduced packing density implies that pyrrole-2-carboxylate occupies a substantially larger surface area per molecule than proline, which is perhaps surprising given that there is no a priori reason to expect pyrrole-2-carboxylate to be significantly the bulkier of the two species. We also note that pyrrole-2-carboxylate is capable of dimerizing by means of H-bonding interactions between carboxylate O atoms and the amine group [40]. Whilst it is beyond the scope of the STM data to determine any detailed model for the molecular motif, the observed pattern of nearest-neighbour pairing is certainly strongly suggestive of some form of dimerization.

In that regard, it is relevant that the two mirror domains appear to occur with equal areas (the two sets of spots are equally bright in the LEED pattern). If achiral objects self-assemble to form a chiral structure, one expects to see equal areas of both mirror domains of that structure—as seen, for example, for the  $(\sqrt{7} \times \sqrt{7})\text{R}19^\circ$  structure formed by  $\text{NO}_2/\text{CO}$  coadsorption on  $\text{Au}\{111\}$  [41]. Pyrrole-2-carboxylate is

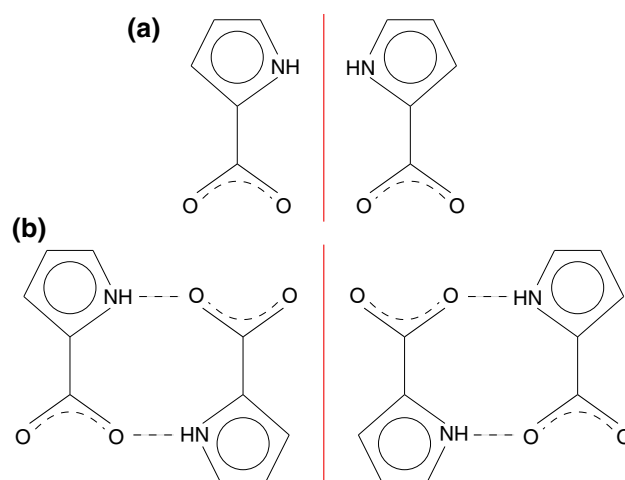


**Fig. 19** **a** The two enantiomers of the pyrrole-2-carboxylate/surface complex. **b** The two enantiomers of the pyrrole-2-carboxylate dimer/surface complex. The grey shading represents the surface plane of the substrate; the red lines are mirror planes

achiral, with a mirror plane running through the plane of the molecule. If the molecule adsorbs with the molecular plane parallel to the surface, it can do so in either of two ways, corresponding to one or other side of the molecule being in contact with the surface (Fig. 19a). These two adsorbate–substrate bonding configurations are chiral, with the amine group lying to one or other side of the molecular axis running from the carboxylate group to the pyrrole ring. Dimerization requires both adsorbates to be bonded as the same enantiomer of the adsorbate–surface complex (Fig. 19b): chirality is preserved in the resulting dimer–surface complex. We infer that the two mirror domains correspond to the two enantiomers of this dimer–surface complex. Given the single-enantiomer L-proline starting point, the equal areas of the two mirror domains imply that as proline dehydrogenates, it passes through a prochiral intermediate with the ring perpendicular to the surface; the resulting pyrrole-2-carboxylate then has equal probability of adopting either of the two possible adsorbate–substrate bonding enantiomers.

After annealing to 510 K, LEED indicates essentially  $(1 \times 1)$  periodicity (albeit with diffuse half-order spots visible at 19 eV); the RAIR spectrum is featureless, but STM clearly shows a disordered adsorbate overlayer with relatively high apparent coverage. Qualitatively, this has the appearance of a molecular (rather than atomic) overlayer, in that the visible features appear larger and less regular than is the case in typical atomic phases, despite having annealed to temperatures where ordered atomic phases (including those involving substrate reconstruction) typically form on Cu surfaces. This implies further dissociation of pyrrole carboxylate to simpler fragments, in orientations that render them RAIRS-inactive, and with sufficient disorder that no clear overlayer periodicity is apparent in LEED.

## 5 Conclusion

The behaviour of L-proline after adsorption on Cu{311} has substantive features in common with that previously observed with alanine and glycine on the same surface [27, 29–31]: specifically, the (2,1;1,2) periodicity characteristic of  $\mu_3$  bonding and associated with the absence of footprint chirality, and a similar transition from pure  $\mu_3$  bonding at low exposures to a mixture of  $\mu_3$  and  $\mu_2$  bonding at higher exposures.

There are, however, significant differences. These include the systematics of the behaviour of the  $\nu(\text{C}=\text{O})$  RAIRS absorption band with exposure and subsequent annealing, and its relationship to structures and structural changes seen in LEED and STM. Although these differences are not fully understood as yet, it is likely that they stem, at least in part, from the impact of the bulky pyrrolidine ring on the kinetics. There are also differences in the internal structure(s) of the characteristic  $[1\bar{3}0]$ -oriented translational domain boundaries with proline as compared to alanine and glycine; moreover, the reorientation of these boundaries towards the  $[2\bar{3}\bar{3}]$  direction when the proline overlayer is annealed has no parallel in the behaviour of alanine or glycine overlayers.

We suggest that the new structural phase with (5,3;4,6) periodicity that emerges on annealing to 480–490 K consists of pyrrole-2-carboxylate, formed by dehydrogenation of proline. The lattice chirality of this structure indicates that it involves a single adsorbate–substrate bonding enantiomer, most likely in an arrangement involving dimerization. The fact that both of the possible mirror domains area observed, with equal areas, implies the involvement of a prochiral intermediate in the conversion from L-proline to pyrrole-2-carboxylate.

**Acknowledgments** The Engineering and Physical Sciences Research Council is acknowledged for financial support.

**Open Access** This article is distributed under the terms of the Creative Commons Attribution 4.0 International License (<http://creativecommons.org/licenses/by/4.0/>), which permits unrestricted use, distribution, and reproduction in any medium, provided you give appropriate credit to the original author(s) and the source, provide a link to the Creative Commons license, and indicate if changes were made.

## References

1. Barlow SM, Kitching KJ, Haq S, Richardson NV (1998) *Surf Sci* 401:322–335
2. Hasselström J, Karis O, Weinelt M, Wassdahl N, Nilsson A, Nyberg M, Pettersson LGM, Samant LG, Stöhr J (1998) *Surf Sci* 407:221–236
3. Booth NA, Woodruff DP, Schaff O, Gießel T, Lindsay R, Baumgärtel P, Bradshaw AM (1998) *Surf Sci* 397:258–269
4. Nyberg M, Hasselström J, Karis O, Wassdahl N, Weinelt M, Nilsson A, Pettersson LGM (2000) *J Chem Phys* 112:5420–5427

5. Chen Q, Frankel DJ, Richardson NV (2002) *Surf Sci* 497:37–46
6. Toomes RL, Kang J-H, Woodruff DP, Polcik M, Kittel M, Hoefl J-T (2003) *Surf Sci* 522:L9–L14
7. Kang J-H, Toomes RL, Polcik M, Kittel M, Hoefl J-T, Efstathiou V, Woodruff DP, Bradshaw AM (2003) *J Chem Phys* 118:6059–6071
8. Nyberg M, Odelius M, Nilsson A, Pettersson LGM (2003) *J Chem Phys* 119:12577–12585
9. Rankin RB, Sholl DS (2004) *Surf Sci* 548:301–308
10. Rankin RB, Sholl DS (2005) *J Phys Chem B* 109:16764–16773
11. Williams J, Haq S, Raval R (1996) *Surf Sci* 368:303–309
12. Barlow SM, Louafi S, Le Roux D, Williams J, Muryn C, Haq S, Raval R (2004) *Langmuir* 20:7171–7176
13. Barlow SM, Louafi S, Le Roux D, Williams J, Muryn C, Haq S, Raval R (2005) *Surf Sci* 590:243–263
14. Haq S, Massey A, Moslemzadeh N, Robin A, Barlow SM, Raval R (2007) *Langmuir* 23:10694–10700
15. Rankin RB, Sholl DS (2005) *Surf Sci* 574:L1–L8
16. Sayago DI, Polcik M, Nisbet G, Lamont CLA, Woodruff DP (2005) *Surf Sci* 590:76–87
17. Jones G, Jones LB, Thibault-Starzyk F, Seddon EA, Raval R (2006) *Surf Sci* 600:1924–1935
18. Zhao X, Gai Z, Zhao RG, Yang WS, Sakurai T (1999) *Surf Sci* 424:L347–L351
19. Efstathiou V, Woodruff DP (2003) *Surf Sci* 531:304–318
20. Mae K, Morikawa Y (2004) *Surf Sci* 553:L63–L67
21. Zhao X, Zhao RG, Yang WS (1999) *Surf Sci* 442:L995–L1000
22. Iwai H, Tobisawa M, Emori A, Egawa C (2005) *Surf Sci* 574:214–218
23. Iwai H, Egawa C (2009) *Langmuir* 26:2294–2300
24. Gladys MJ, Stevens AV, Scott NR, Jones G, Batchelor D, Held G (2007) *J Phys Chem* 111:8331–8336
25. Thomsen L, Wharmby MT, Riley DP, Held G, Gladys MJ (2009) *Surf Sci* 603:1253–1261
26. Eralp T, Shavorskiy A, Zheleva ZV, Dhanak VR, Held G (2010) *Langmuir* 26:10918–10923
27. Clegg ML, Morales de la Garza L, Karakatsani S, King DA, Driver SM (2011) *Top Catal* 54:1429–1444
28. Clegg ML, Driver SM, Blanco-Rey M, King DA (2010) *J Phys Chem C* 114:4114–4117
29. Madden DC, Bentley ML, Jenkins SJ, Driver SM (2014) *Surf Sci* 629:81–87
30. Madden DC, Temprano I, Sacchi M, Blanco-Rey M, Jenkins SJ, Driver SM (2014) *J Phys Chem C* 118:18589–18603
31. Madden DC, Temprano I, Sacchi M, Jenkins SJ (2015) *J Phys Chem C*. doi:10.1021/acs.jpcc.5b02349
32. Mateo Marti E, Barlow SM, Haq S, Raval R (2002) *Surf Sci* 501:191–202
33. Forster M, Dyer MS, Persson M, Raval R (2009) *J Am Chem Soc* 131:10173–10181
34. Forster M, Dyer MS, Persson M, Raval R (2010) *Angew Chem Int Ed* 49:2344–2348
35. Leibsle FM, Flipse CFJ, Robinson AW (1994) *Phys Rev B* 47:15865–15868
36. Leibsle FM, Dhessi SS, Barrett SD, Robinson AW (1994) *Surf Sci* 317:309–320
37. Driver SM, Hoefl J-T, Polcik M, Kittel M, Terborg R, Toomes RL, Kang J-H, Woodruff DP (2001) *J Phys Condens Matter* 13:L601–L606
38. Driver SM, Woodruff DP (2001) *Surf Sci* 492:11–26
39. Masuda T, Barnes CJ, Hu P, King DA (1992) *Surf Sci* 276:122–138
40. Grabowski SJ, Dubis AT, Martynowski D, Głowka M, Palusiak M, Leszczynski J (2004) *J Phys Chem A* 108:5814–5822
41. Zhang T, King DA, Driver SM (2012) *J Chem Phys* 137:074703-1-5